NANO LETTERS

Letter

pubs.acs.org/NanoLett

# Electron Doping of Ultrathin Black Phosphorus with Cu Adatoms

Steven P. Koenig,[†,‡] Rostislav A. Doganov,[†,‡,§] Leandro Seixas,[†,‡] Alexandra Carvalho,[†,‡] Jun You Tan,[†,‡] Kenji Watanabe,[∥] Takashi Taniguchi,[∥] Nikolai Yakovlev,[⊥] Antonio H. Castro Neto,[†,‡,§] and Barbaros Özyilmaz*[,†,‡,§]

[†]Centre for Advanced 2D Materials, National University of Singapore, 6 Science Drive 2, Singapore 117546, Singapore

[‡]Department of Physics, National University of Singapore, 2 Science Drive 3, Singapore 117542, Singapore

[§]Graduate School for Integrative Sciences and Engineering (NGS), National University of Singapore, 28 Medical Drive, Singapore 117456, Singapore

[∥]National Institute for Materials Science, 1-1 Namiki, Tsukuba 305-0044, Japan

[⊥]Institute of Materials Research and Engineering (IMRE), Agency for Science, Technology and Research, 2 Fusionopolis Way, Singapore 138634, Singapore

Supporting Information

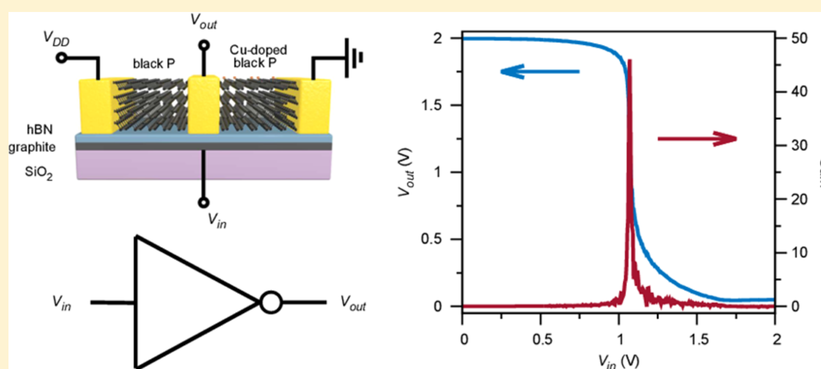


**ABSTRACT:** Few-layer black phosphorus is a monatomic two-dimensional crystal with a direct band gap that has high carrier mobility for both holes and electrons. Similarly to other layered atomic crystals, like graphene or layered transition metal dichalcogenides, the transport behavior of few-layer black phosphorus is sensitive to surface impurities, adsorbates, and adatoms. Here we study the effect of Cu adatoms onto few-layer black phosphorus by characterizing few-layer black phosphorus field effect devices and by performing first-principles calculations. We find that the addition of Cu adatoms can be used to controllably n-dope few layer black phosphorus, thereby lowering the threshold voltage for n-type conduction without degrading the transport properties. We demonstrate a scalable 2D material-based complementary inverter which utilizes a boron nitride gate dielectric, a graphite gate, and a single bP crystal for both the p- and n-channels. The inverter operates at matched input and output voltages, exhibits a gain of 46, and does not require different contact metals or local electrostatic gating.

**KEYWORDS:** *Phosphorene, black phosphorus, transistor, inverter, adatoms, doping*

Two-dimensional (2D) van der Waals materials have attracted significant attention since the rise of graphene for applications in electronic,[1] optoelectronic,[2] and thermoelectric devices.[3] In particular, 2D materials have shown great promise for application in flexible electronics and optoelectronics where 2D atomic crystals have the potential to supplant organic semiconductors due to their superior mobility and ultimate flexibility.[4−6] Thus, far layered transition metal dichalcogenides (TMDCs), in particular $MoS_2$,[7] have been the most widely studied of the 2D semiconducting materials. However, $MoS_2$, $WS_2$, and other TMDCs have a strong natural propensity toward unipolar field effect transistor (FET) operation, which makes it difficult to achieve stable high-mobility p-type and n-type conduction in the same material. For example, $MoS_2$ has a strong tendency to be n-type due to a low-lying valence band and native defects such as sulfur vacancies.[8,9] On the other hand, a large number of practical semiconductor devices, such as logic gates, photodiodes, light-emitting diodes, and solar cells, require both p-type and n-type unipolar operation, achieved in the same parent semiconducting material. $WSe_2$ is one TMDC that shows ambipolar behavior, although it remains difficult to make good electrical contact for both electron and hole injection.[10] Strategies to modulate the carrier type in 2D materials by metal work-

Received: August 16, 2015
Revised: February 17, 2016
Published: March 3, 2016

ACS Publications © 2016 American Chemical Society

function engineering or local electrostatic gating are of limited practical relevance, while substitutional doping, for example, as in $MoS_2$:Nb, has so far not resulted in high mobility transport for the complementary carrier type.[11]

Recently, ultrathin black phosphorus (bP), or phosphorene, has emerged as an exciting addition to the field of 2D semiconductor materials.[12−16] Phosphorene, the second monotypic van der Waals 2D material to be investigated, has a band gap that allows for both larger on−off ratio than in graphene FETs and higher mobility than in TMDCs, along with nearly symmetric transport characteristics for p-type and n-type conduction.[17] To make use of few-layer bP in practical applications, control over the electronic, magnetic, and thermal properties is required. To date, studies have focused mainly on the effect of dielectric capping layers for passivation and top gating of few-layer bP devices, such as atomic layer deposited $Al_2O_3$ and $HfO_2$ as well as and dry transferred hBN.[18−25] One recent report used $MoO_3$ and $CsCO_3$ to dope few-layer bP through surface charge transfer.[26] A number of theoretical studies have studied the effect of adsorbed and impurity atoms on the properties of bP.[27−34] A subset of these studies have focused on the effect of metal adatoms on single layer phosphorene as a means to tune the electronic[30,31] and magnetic[32−34] properties, which in particular could be used to modulate the charge carrier type. Being more reactive than graphene, phosphorene can form strong bonds with adsorbed atoms,[31] while the weak p-type propensity can allow for high n-type conduction, resulting in stable high-mobility p-type and n-type FETs in the same 2D material. To date, no study has experimentally demonstrated the use of metal adatoms to modulate the charge carrier type in bP.

In this Letter, we study the effect of Cu adatoms on the electronic properties of few-layer bP. To understand the role of Cu adatoms, we performed first-principle calculations on four-layer bP. For the four-layer system, we looked both at Cu adatoms bonded to the top surface and Cu atoms intercalated into the few-layer crystal. In both cases, the Cu atom acts as an electron donor and n-dopes the ultrathin bP without perturbing the structural integrity of the crystal. We conducted electrical transport studies to experimentally probe that the addition of Cu atoms electron dopes the bP and lowers the threshold voltage for electron conduction, thereby modulating the polarity of the channel from p-type to n-type. We then used Cu doping of bP to fabricate a CMOS-like inverter with an undoped p-channel and a Cu doped n-channel. The inverter demonstrated here uses a single contacting metal, is fabricated from a single exfoliated bP crystal, and does not require local electrostatic gating to define the p-type and n-type channels.

First, we turn to the numerical results for the band structure of Cu-doped bP. The first-principles calculations are based on density functional theory (DFT)[35,36] as implemented in SIESTA package.[37] We studied the effect of two possible Cu impurities on the band structure of few-layer bP. The two impurities are Cu atoms adsorbed on the topmost bP layer (referred to as $Cu_{ad}$) and Cu impurities intercalated between the second and third layers ($Cu_{int}$) of four-layer bP. The two geometries are illustrated in Figure 1a. Both impurities are found to be at local minima with binding energies of $E_b[Cu_{ad}]$ = −2.62 eV and $E_b[Cu_{int}]$ = −3.32 eV. The band structures of pristine bP, bP with the $Cu_{ad}$, and bP with the $Cu_{int}$ configurations are shown in Figure 1c. All energies are given with relation to the vacuum level. For pristine bP, we observe a workfunction of 4.38 eV, which is close to the value for

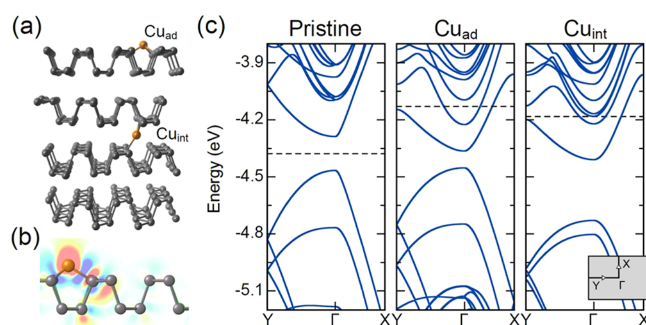


**Figure 1.** (a) Schematic drawing of the two defects studied here: surface adsporbed $Cu_{ad}$ and interstitial, $Cu_{int}$. (b) Charge density difference of the $Cu_{ad}$. The red and blue regions refer to electron depletion ($\Delta\rho = -2 \times 10^{-3}\ e/a_0^3$) and accumulation ($\Delta\rho = +2 \times 10^{-3}\ e/a_0^3$), respectively. (c) Calculated band structure of pristine four-layer bP, four layer bP with adsorbed Cu, ($Cu_{ad}$), and four layer bP with interstitial Cu ($Cu_{int}$). The dashed line indicates the Femi level for each case.

monolayer phosphorene[38] and a Fermi level in the middle of the band gap. In both the adatom and interestitial configurations, the Cu impurity donates one electron and shifts the Fermi level of bP into the conduction band. This is in agreement with what is reported in ref 28 for the phosphorene monolayer. The huge Fermi level shift in Figure 1c is due to the finite size of the bP cell used in the calculation, which leads to a large Cu concentration in the system. The donated electron originates from the Cu 4s shell, leaving a stable, closed-shell $Cu^+$ cation. In Figure 1b, we show the charge-density difference, $\Delta\rho = \rho_{Cu+bP} - \rho_{bP} - \rho_{Cu}$, of the $Cu_{ad}$−bP system. Here $\rho_{Cu+bP}$, $\rho_{bP}$, and $\rho_{Cu}$ are the total charge densities of, respectively, the $Cu_{ad}$−bP system, pristine bP, and the isolated Cu atom. In the $Cu_{ad}$ configuration, the band gap is reduced to 0.09 eV compared to 0.18 eV in the pristine case due to an internal electric field.[39] For the intercalated $Cu_{int}$ configuration, besides the n-type doping the distance between the two bP layers increases, "decoupling" the system into two bP bilayers. This then leads to an increase of the band gap from 0.18 to 0.32 eV. Even though the Perdew−Burke−Ernzerhof (PBE) band gap is systematically underestimated, it usually reproduces well changes originated by small perturbations, as in the case considered here. The band structure calculations show that both adsorbed and interstitial Cu atoms are n-type dopants, but change the band gap energy in opposite ways. Most importantly, both $Cu_{ad}$ and $Cu_{int}$ have large binding energies while preserving the structural integrity and band structure near the edges of the conduction and valence bands.

We now move to the experimental results and study the effect of Cu adatoms on few-layer bP field effect devices. Cu adatoms were deposited in a DC sputtering system for 1 s at a pressure of 2 mTorr and a DC power of 60 W. The tenuous Cu treatment at a low rate and short deposition time does not allow the formation of continuous Cu islands or Cu clusters on the crystal surface. Atomic force microscopy (AFM) of the surface of an exfoliated few-layer bP crystal after Cu deposition is shown in Figure 2a. The surface topology and measured root-mean-square roughness of $R$ = 0.193 nm are characteristic of exfoliated bP[21] and air sensitive 2D crystals[40] and do not indicate the presence of Cu structures. Cu was also deposited via thermal deposition which resulted in clusters of Cu atoms (see Figure S1 of the Supporting Information). Because the sputtered Cu resulted in a more uniform distribution of Cu, we


DOI: 10.1021/acs.nanolett.5b03278
Nano Lett. 2016, 16, 2145−2151

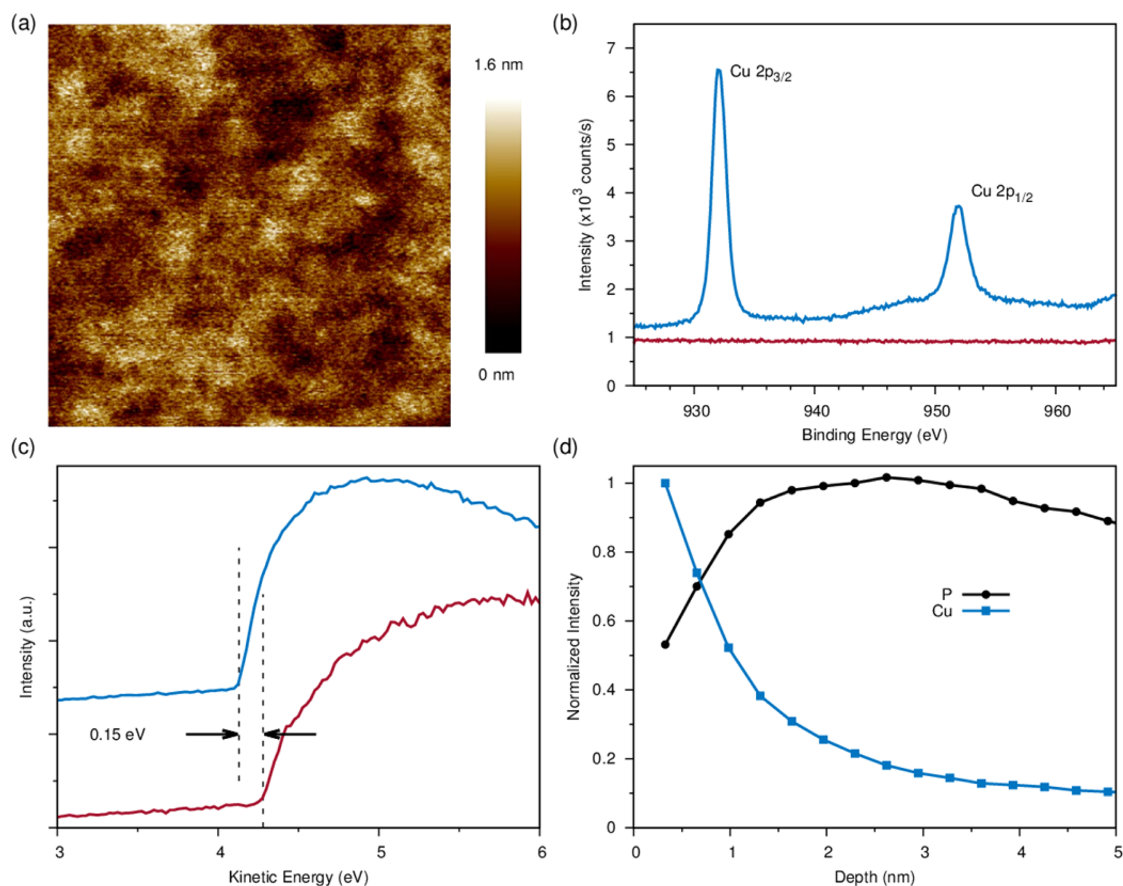


**Figure 2.** (a) AFM scan of a 7.5 nm thick bP crystal after sputtered deposition of Cu adatoms. AFM scan size is 750 nm × 750 nm. (b) XPS spectra of bulk bP with (blue) and without (red) Cu sputtering treatment. (c) UPS spectra of bulk bP with (blue) and without (red) Cu sputtering. The dashed lines show the SECO. (d) ToF-SIMS of exfoliated bP treated with sputtered Cu. The black and blue symbols show the intensity of the ToF-SIMS signal versus sample depth for the P and $^{63}$Cu ions, respectively. The signal is normalized to the maximum measured intensity for the particular ion.

made that the focus of further characterization. Although no clustering was seen in sputtered Cu, clear signatures of elemental Cu on the bP surface can be detected using X-ray photoelectron spectroscopy (XPS). Figure 2b shows the XPS spectrum of an untreated and Cu-treated bulk bP crystal in the region between 925 and 965 eV. The spectrum clearly shows the presence of Cu atoms on the crystal surface by the emergence of peaks at 932 and 958 eV after Cu deposition. Furthermore, ultraviolet photoelectron spectroscopy (UPS), performed together with the XPS measurement, shows a difference in the value of the work function between the untreated and Cu treated bP. Figure 2c shows the onset of the secondary photoelectrons also known as the secondary electron cutoff (SECO). The onset energy directly yields the work function because the SECO corresponds to the vacuum level of the sample with respect to the Fermi energy. The UPS spectrum in Figure 2c shows a decrease of the work function by $\Delta E$ = 0.15 eV in the Cu treated sample, which is attributed to the electron doping of the bP surface by the deposited Cu atoms.

To further characterize the deposition of Cu atoms on exfoliated crystals, we performed time-of-flight secondary ion mass spectroscopy (ToF-SIMS). Cu treated few-layer bP crystals exfoliated onto $SiO_2$/Si wafers were placed in a SIMS apparatus and studied using positive secondary ions ejected by a 25 kV Bi primary beam. The ToF technique allow us to obtain the SIMS signal at different etching times, thereby providing a depth profile of the detected elements. Figure 2d shows the relative intensity versus sample depth for $^{63}$Cu and P ions obtained from a Cu-treated exfoliated few-layer bP. The intensity of the $^{63}$Cu signal clearly decreases with depth, and an exponential fit gives an approximate penetration depth of 1 nm. The P signal increases with depth up to about 3 nm beyond which slowly starts decreasing, likely due to the limited thickness of the few-layer bP crystal. The ToF-SIMS measurement confirms that the majority of deposited Cu remains on the top surface of the exfoliated bP and indicates that the energetic sputtering process does not lead to significant substitutional Cu doping.

We now turn to the transport properties of Cu-doped field effect devices. FETs were fabricated from few-layer crystals exfoliated onto Si wafers with 300 nm $SiO_2$ or dry transferred onto hexagonal boron nitride (hBN).[41] The wafers were prepatterned with alignment markers to minimize the processing time and reduce air exposure. Electron beam lithography (EBL) followed by thermal evaporation, and liftoff was used to fabricate electrical contacts of Ti and Au (5 and 70 nm, respectively). Before characterization, the samples were annealed in situ under high vacuum ($<5 \times 10^{-7}$ Torr) at 400 K for 1 h to reduce hysteresis and remove doping from the ambient degradation and fabrication residue.[21,42] After annealing, the samples were characterized under high vacuum

using a DC four-point measurement at room temperature and down to 5 K. Figure 3a shows the optical image of a 10 nm thick bP sample transferred onto 30 nm of hBN. AFM and thickness measurements of the bP sample can be seen in parts b and c of Figure 3, respectively. The four-point conductance, $G$, versus backgate voltage, $V_g$, of the sample before Cu treatment and at room temperature is shown in Figure 3d. The field effect mobility is extracted using

$$\mu_{FE} = \frac{L}{W}\frac{1}{C_g}\frac{dG}{dV_g}$$

where $L = 2.4$ $\mu$m and $W = 8.8$ $\mu$m are the channel length and width, respectively, and $C_g$ is the gate capacitance. After annealing and prior to Cu adatom deposition, the device exhibits a hole mobility of $\mu_{FE}$ = 690 $cm^2V^{-1}s^{-1}$ at room temperature and up to $\mu_{FE}$ = 1780 $cm^2$ $V^{-1}$ $s^{-1}$ at low temperatures, as shown in Figure 3e. Hole mobilities are taken at $n_h = 3.0 \times 10^{12}$ $cm^{-2}$. The electron mobility of the annealed device, prior to Cu treatment, is 340 $cm^2$ $V^{-1}$ $s^{-1}$ at room temperature and reaches a maximum of 580 $cm^2$ $V^{-1}$ $s^{-1}$ at 150 K, taken at $n_e = 2.5 \times 10^{12}$ $cm^{-2}$. After the initial characterization, the samples were taken out of the measurement probe to a UHV DC sputtering system to deposit Cu atoms using the aforementioned deposition conditions. The samples were then moved back into the vacuum measurement probe and annealed again for 1 h at 400 K to remove adsorbed oxygen and water that might accumulate while moving the device between the two systems in ambient air and which are known p-dopants of few-layer bP.[21,42,43] After Cu deposition, the electron mobility increased to 380 $cm^2$ $V^{-1}$ $s^{-1}$ at room temperature and 2140 $cm^2$ $V^{-1}$ $s^{-1}$ at 7 K (at $n_e = 3.2 \times 10^{12}$ $cm^{-2}$), while the hole mobility decreased to 570 $cm^2$ $V^{-1}$ $s^{-1}$ at 300 K (at $n_h = 3.0 \times 10^{12}$ $cm^{-2}$) but remained relatively unchanged at low temperature as shown in Figure 3e (see

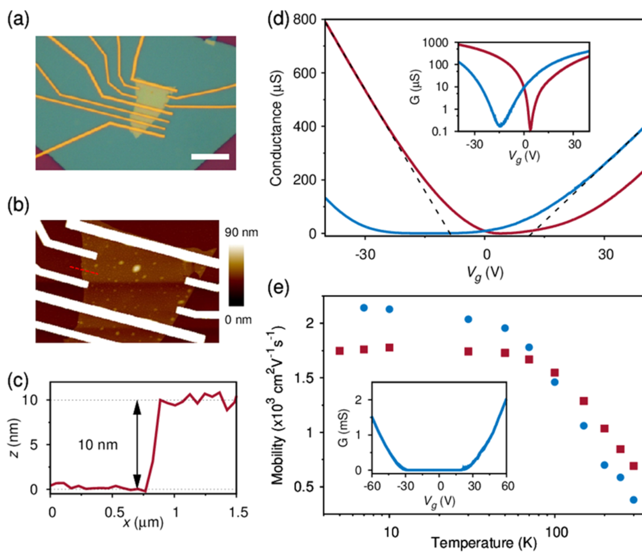


**Figure 3.** (a) Optical image of the 10 nm bP crystal on top of hBN measured before and after Cu treatment. The scale bar is 10 $\mu$m. (b) AFM image of the channel measured, with the line cut in (c) showing the height of the bP. The AFM image is 16 $\mu$m wide. (d) Four-point conductance versus gate voltage, $V_g$, at room temperature before (red) and after (blue) Cu doping. The inset shows the same data on a logarithmic scale. The black dashed lines show the fits used for extracting the mobility. (e) Temperature dependence of the hole field effect mobility before Cu doping (red symbols) and the electron mobility after Cu doping (blue symbols). The inset shows the conductance versus backgate voltage after Cu doping at $T$ = 7 K.

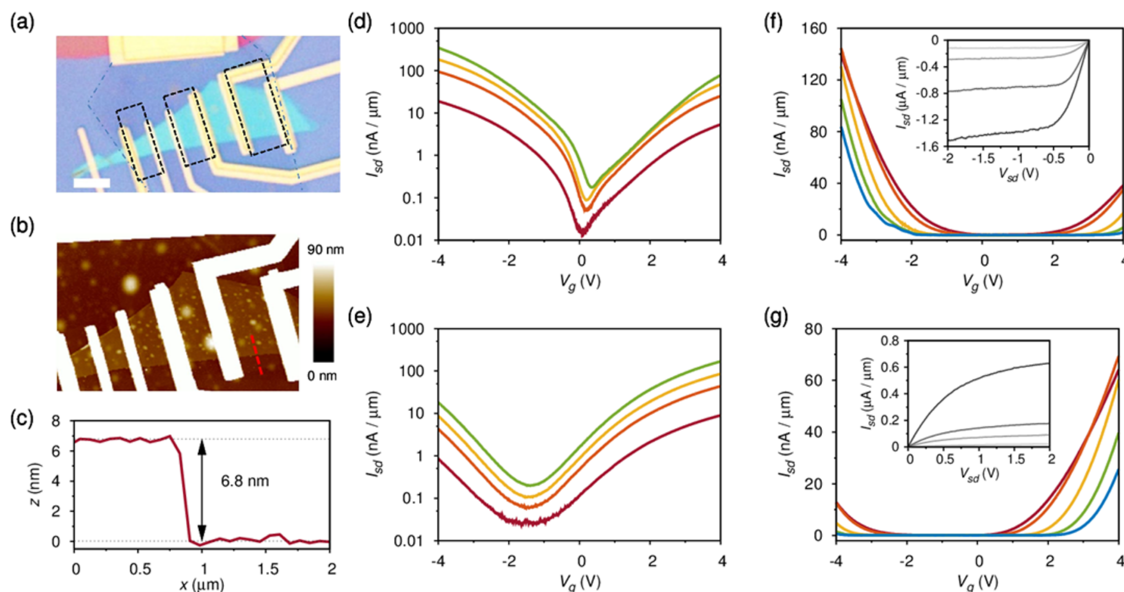


**Figure 4.** (a) Optical image of the device. The black boxes outline the areas that were treated with sputtered Cu. Scale bar is 5 $\mu$m (b) AFM image and (c) line cut taken from (b) showing the flake thickness. (d,e) Two-point source drain current, $I_{sd}$, versus gate voltage, $V_g$, at room temperature for $V_{sd}$ values of 10, 50, 100, and 200 mV for the undoped bP p-FET and Cu doped bP n-FET, respectively (f) Two-point source drain current, $I_{sd}$, versus gate voltage, $V_g$, at $V_{sd}$ of 10 mV of the undoped bP p-FET at temperatures of 250, 200, 100, 50, and 30 K with the colors going from red to blue. The inset shows the $I_{sd}-V_{sd}$ characteristics at 300 K for $V_g$ from −0.5 V (lightest gray) to −2.5 V (darkest gray) in steps of 0.5 V. (g) Two-point source drain current, $I_{sd}$, versus gate voltage, $V_g$, at $V_{sd}$ of 10 mV for the Cu doped bP n-FET at temperatures of 250, 200, 100, 50, and 30 K, with the colors going from red to blue. The inset shows the $I_{sd}-V_{sd}$ characteristics at 300 K for $V_g$ from 0.5 V (lightest gray) to 2.5 V (darkest gray) in steps of 0.5 V.


DOI: 10.1021/acs.nanolett.5b03278
Nano Lett. 2016, 16, 2145−2151

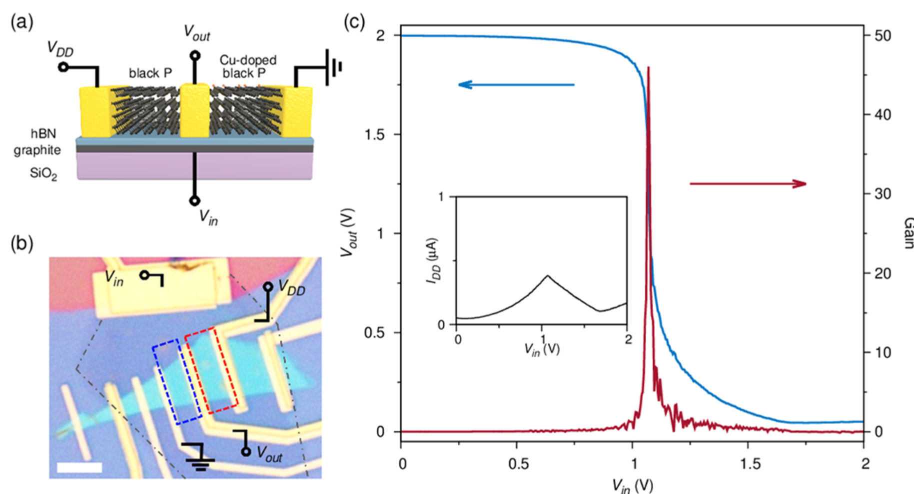


**Figure 5.** (a) Schematic of the bP inverter fabricated using an untreated p-FET channel and a Cu doped n-FET channel. The heterostructure consist of a 6 nm thick graphite bottom gate, used as $V_{in}$, a 30 nm thick hBN gate dielectric, and a single 7 nm bP flake with Ti/Au contacts sitting on an $SiO_2$ substrate. (b) Optical image of the device. The gray dash−dot line outlines the graphite bottom gate, and the red and blue boxes mark the p-FET channel and Cu doped n-FET channel, respectively. The scale bar is 5 μm. (c) Output voltage, $V_{out}$, versus input voltage, $V_{in}$, of the inverter at $V_{DD}$ = 2 V. The inverter gain versus $V_{in}$ is shown in red on the right axis. The inset shows the device current, $I_{DD}$, versus $V_{in}$.

Supporting Information, Figure S3). The low temperature electron mobility is the highest measured in few-layer bP, indicating that the addition of Cu adatoms does not degrade the transport quality in the crystal. Similar results were repeated with Cu deposited by both sputtering and thermal evaporation, see Supporting Information, Figure S4. The inset of Figure 3d shows the conductance versus $V_g$ on the logarithmic scale. From the logarithmic plot we extracted a shift in threshold voltage, $V_{th}$, after Cu adatom deposition, see Methods. The shift $\Delta V_{th}$, is −22.4 V for the hole side and −13.8 V for the electron side. The average shift $\Delta V_{th}$ for electrons and holes is −18.1 V, which corresponds to the addition of 12.7 × $10^{11}$ electrons/$cm^2$. Doping by metal adatoms is not specific to Cu and has been studied theoretically for both Ag and Au adatoms on phosphorene.[31] To demonstrate the versatility of metal adatom doping, Ag and Au metal adatoms were deposited onto bP FETs. The transport properties were measured and are shown in Supporting Information, Figure S6. Consistent with previous theory, Ag electron dopes the bP while Au is a hole dopant.[31] This opens up the ability to further tailor bPs doping with the addition of other adatoms similar to doping in conventional semiconductors such as Si. A total of four devices with Cu doping were measured here, all showing a negative shift in the threshold voltage

The control of the channel doping and threshold voltage of few-layer bP by Cu adatoms offers a scalable route for making all-bP complementary logic devices without the need of different contact metals or constant local electrostatic gating.[44−46] To this end, we fabricated a 2D complementary inverter using a 30 nm thick hexagonal BN (hBN) gate dielectric, a 6 nm graphite gate, and a single 7 nm bP crystal for both the p- and n-channels. The fabrication consists of exfoliating graphite on a $SiO_2$ wafer, followed by stacking of hBN and few-layer bP in two dry transfer steps. After lithography and thermal evaporation of the metal electrodes, an additional mask was patterned using EBL and Cu was deposited on one of the bP channels so that the final device consists of one Cu-doped and one untreated channel on the same ultrathin crystal, see Figure 4a for the optical image of the device, with the black boxes indicating where Cu was deposited. Figure 4b shows the AFM image while the AFM cross section can be seen in Figure 4c. Once loaded into the probe, the device was annealed for 1 h at 400 K. The two-point device characteristics of the p-channel and Cu doped n-channel of the inverter can be seen in Figure 4d,f for the p-channel and Figure 4e,g for the Cu doped n-channel (see Methods for channel dimensions). The room temperature two-point source drain current, $I_{sd}$, versus $V_g$ taken at room temperature at $V_{sd}$ = 10, 50, 100, and 200 mV can be seen in parts d and e of Figure 4 for the p-channel and Cu doped n-channel, respectively. The two-point source drain current, $I_{sd}$, versus $V_g$, taken at $V_{sd}$ = 10 mV in Figure 4b, shows that the addition of Cu adatoms results in consistent n-type operation of the FET at all measured temperatures. In the insets of Figure 4f ,g, we show the $I_{sd}$−$V_{sd}$ curves of the two FETs at room temperature for $|V_g|$ from 1 to 2.5 V in steps of 0.5 V. The $I$−$V$ characteristics exhibit saturation behavior in both the hole and electron channels. We now turn to characterizing the two FETs combined in a complementary inverter as shown in the schematic in Figure 5a.

The inverter was measured at room temperature with a power supply voltage of $V_{DD}$ = 2 V. As the input voltage at the graphite gate, $V_{in}$, was swept from 0 to 2 V, the output voltage at the middle terminal, $V_{out}$, switched from 1.99 V at $V_{in}$ = 0 V to a low voltage of 0.04 V at $V_{in}$ = 2 V. The gain of the inverter, defined by $g = dV_{out}/dV_{in}$, was found to be $g$ = 46, see Figure 5b. The inverter gain was stable over 10 days of measuring in vacuum and at elevated temperatures of up to 330 K, see Supporting Information, Figure S9. The noise margins of the inverter were found to be $NM_H = 0.30V_{DD}$ for the high input voltage and $NM_L = 0.37V_{DD}$ for the low input voltage. The noise margin above 30% of $V_{DD}$ shows that the device has a high noise tolerance and can be integrated into a large multistage inverter system. The DC current drawn from the power supply, $I_{DD}$, versus $V_{in}$ is shown in the inset of Figure 5b. The current increases around the switching voltage $V_{in}$ = 1 V and for $V_{in}$ > 1.6 V One limitation of the demonstrated device is that after annealing the pristine p-channel still exhibits some ambipolar operation, leading to a nonzero $I_{DD}$ at $V_{in}$ = 2 V. Additional hole doping of the p-channel will be required to reduce this unwanted current flow. This could potentially be


DOI: 10.1021/acs.nanolett.5b03278
Nano Lett. 2016, 16, 2145−2151

improved by introducing metal adatoms which lead to hole doping, as, for example, with Au adatoms.[31]

In summary, we studied the effect of Cu adatoms on few-layer bP by first-principles DFT calculations and charge transport measurements. Using first-principles DFT calculations, Cu was shown to be an excellent electron donor for few-layer bP in both the adatom and interstitial configurations. In charge transport measurements, sputtered Cu was shown to electron dope few-layer bP and shift the threshold voltage, thereby converting the bP channel from a predominantly p-type with a hole mobility of 690 $cm^2 V^{-1} s^{-1}$ to n-type with electron mobility of 380 $cm^2 V^{-1} s^{-1}$ at room temperature. We observed a record high electron mobility of 2140 $cm^2 V^{-1} s^{-1}$ at low temperature, which shows that the doping method does not degenerate the transport properties. Finally, we demonstrated an ultrathin bP inverter fabricated using an hBN gate dielectric and graphite bottom gate. The 2D complementary inverter uses a single exfoliated bP crystal with an untreated p-channel and Cu doped n-channel, operates at 2 V with matched input and output voltages, and exhibits a gain of 46. This work shows the potential of using metal adatoms to locally tune the properties of bP for logic applications without the need of different contact metals or local electrostatic gating.

**Methods.** Bulk crystals were purchased from HQ graphene. ToF-SIMS was carried out using $Bi^+$ ions accelerated at 25 kV and a beam current of 0.6 pA with a 50 $\mu$m spot size. The sputtering rate for ToF-SIMS was 1 nm per 100 s. Electron beam lithography was carried out on a JEOL JBX-6300FS. Ti+Au metal contact electrodes were deposited using thermal evaporation at a rate of 1 Å/s. AFM measurements were taken on a Bruker Dimension FastScan. DC four-point measurements were carried out under high vacuum ($<5 \times 10^{-7}$ Torr) with a Keithley model 2400 source meter in Ohms mode and Keithley model 6430 for two-point DC measurements. For transport measurements, we took the threshold voltage, $V_{th}$, as the gate voltage, $V_g$, at which the conductance is at 1 $\mu$S. The 2-point data from the p- and n-channels shown in Figure 4 are taken from the respective channels highlighted in Figure 5b with the channel dimensions ($L \times W$) being 1.8 $\mu$m × 6.6 $\mu$m and 2.25 $\mu$m × 4.7 $\mu$m for the p- and n-channels, respectively.

*Theoretical Methods.* Our computational approach to study the equilibrium structure, stability, and electronic structure of Cu doped bP is based on density functional theory (DFT)[35,36] as implemented in SIESTA package.[37] We used DZP localized basis, norm-conserved pseudopotentials with Troullier–Martins parametrization,[47] mesh cutoff energy of 350 Ry, and $k$-points sampling of Brillouin zone in Monkhorst–Pack algorithm[48] with 10 × 10 × 1 grid. The exchange-correlation functional used is based on PBE generalized-gradient approximation.[49] We included van der Waals forces in Grimme approximation[50] in order to describe the interaction between bP layers. The calculations were performed within a supercell framework with 3 × 3 unit cells and four bP layers.

## ■ ASSOCIATED CONTENT

### Supporting Information

The Supporting Information is available free of charge on the ACS Publications website at DOI: 10.1021/acs.nanolett.5b03278.

Optical and AFM images and Raman spectrum of devices presented in the text along with additional transport data on Cu, Au, and Ag doped bP (PDF)

## ■ AUTHOR INFORMATION


### Corresponding Author

*E-mail: barbaros@nus.edu.sg.

### Present Addresses

(S.P.K.) Institute of Materials Research and Engineering (IMRE), Agency for Science, Technology and Research, 2 Fusionopolis Way, 138634, Singapore.

(L.S.) MackGraphe - Graphene and Nanomaterials Research Center, Mackenzie Presbyterian University, São Paulo 01302-907, SP, Brazil.

### Author Contributions

S.P.K. and R.A.D. contributed equally.


### Notes

The authors declare no competing financial interest.

## ■ ACKNOWLEDGMENTS

B.Ö. acknowledges support by the National Research Foundation, Prime Minister's Office, Singapore, under its Competitive Research Programme (CRP award no. NRF-CRP9-2011-3) and the SMF-NUS Research Horizons Award 2009-Phase II. A.H.C.N. acknowledges the NRF-CRP award "Novel 2D materials with tailored properties: beyond graphene". The calculations were performed at the CA2DM computing facilities. S.P.K., R.A.D., L.S., A.C., A.H.C.N., and B.O. acknowledge the NRF, Prime Minister's Office, Singapore, under its Medium-Sized Centre Programme. L.S. acknowledges financial support provided by CNPq/Brazil. We thank Srinivasan Natarajan for his help with the device schematic presented in Figure 5. We thank Kuan Henche in the Department of Materials Science and Engineering at NUS for assisting with the XPS and UPS measurements.

## ■ REFERENCES


(1) Fiori, G.; Bonaccorso, F.; Iannaccone, G.; Palacios, T.; Neumaier, D.; Seabaugh, A.; Banerjee, S. K.; Colombo, L. *Nat. Nanotechnol.* **2014**, *9* (10), 768–779.

(2) Koppens, F. H. L.; Mueller, T.; Avouris, P.; Ferrari, a. C.; Vitiello, M. S.; Polini, M. *Nat. Nanotechnol.* **2014**, *9* (10), 780–793.

(3) Buscema, M.; Barkelid, M.; Zwiller, V.; van der Zant, H. S. J.; Steele, G. A.; Castellanos-Gomez, A. *Nano Lett.* **2013**, *13* (2), 358–363.

(4) Zhu, W.; Yogeesh, M. N.; Yang, S.; Aldave, S. H.; Kim, J.; Sonde, S. S.; Tao, L.; Lu, N.; Akinwande, D. *Nano Lett.* **2015**, *15*, 1883–1890.

(5) Akinwande, D.; Petrone, N.; Hone, J. *Nat. Commun.* **2014**, *5*, 5678.

(6) Wang, Q. H.; Kalantar-Zadeh, K.; Kis, A.; Coleman, J. N.; Strano, M. S. *Nat. Nanotechnol.* **2012**, *7* (11), 699–712.

(7) Butler, S. Z.; Hollen, S. M.; Cao, L.; Cui, Y.; Gupta, J. A.; Gutiérrez, H. R.; Heinz, T. F.; Hong, S. S.; Huang, J.; Ismach, A. F.; Johnston-Halperin, E.; Kuno, M.; Plashnitsa, V. V.; Robinson, R. D.; Ruoff, R. S.; Salahuddin, S.; Shan, J.; Shi, L.; Spencer, M. G.; Terrones, M.; Windl, W.; Goldberger, J. E. *ACS Nano* **2013**, *7* (4), 2898–2926.

(8) Das, S.; Chen, H.-Y.; Penumatcha, A. V.; Appenzeller, J. *Nano Lett.* **2013**, *13* (1), 100–105.

(9) Popov, I.; Seifert, G.; Tománek, D. *Phys. Rev. Lett.* **2012**, *108* (15), 156802.

(10) Allain, A.; Kis, A. *ACS Nano* **2014**, *8* (7), 7180–7185.

(11) Suh, J.; Park, T.-E.; Lin, D.-Y.; Fu, D.; Park, J.; Jung, H. J.; Chen, Y.; Ko, C.; Jang, C.; Sun, Y.; Sinclair, R.; Chang, J.; Tongay, S.; Wu, J. *Nano Lett.* **2014**, *14* (12), 6976–6982.

(12) Li, L.; Yu, Y.; Ye, G. J.; Ge, Q.; Ou, X.; Wu, H.; Feng, D.; Chen, X. H.; Zhang, Y. *Nat. Nanotechnol.* **2014**, *9* (5), 372–377.

(13) Koenig, S. P.; Doganov, R. A.; Schmidt, H.; Castro Neto, A. H.; Özyilmaz, B. *Appl. Phys. Lett.* **2014**, *104* (10), 103106.




DOI: 10.1021/acs.nanolett.5b03278
Nano Lett. 2016, 16, 2145–2151

(14) Liu, H.; Neal, A. T.; Zhu, Z.; Luo, Z.; Xu, X.; Tománek, D.; Ye, P. D. *ACS Nano* **2014**, *8* (4), 4033−4041.
(15) Castellanos-Gomez, A.; Vicarelli, L.; Prada, E.; Island, J. O.; Narasimha-Acharya, K. L.; Blanter, S. I.; Groenendijk, D. J.; Buscema, M.; Steele, G. A.; Alvarez, J. V.; Zandbergen, H. W.; Palacios, J. J.; van der Zant, H. S. J. *2D Mater.* **2014**, *1* (2), 025001.
(16) Xia, F.; Wang, H.; Jia, Y. *Nat. Commun.* **2014**, *5*, 4458.
(17) Churchill, H. O. H.; Jarillo-Herrero, P. *Nat. Nanotechnol.* **2014**, *9* (5), 330−331.
(18) Kim, J.-S.; Liu, Y.; Zhu, W.; Kim, S.; Wu, D.; Tao, L.; Dodabalapur, A.; Lai, K.; Akinwande, D. *Sci. Rep.* **2015**, *5*, 8989.
(19) Hong, T.; Chamlagain, B.; Lin, W.; Chuang, H.-J.; Pan, M.; zhou, Z.; Xu, Y.-Q. *Nanoscale* **2014**, *6*, 8978−8983.
(20) Wood, J. D.; Wells, S. A.; Jariwala, D.; Chen, K.-S.; Cho, E.; Sangwan, V. K.; Liu, X.; Lauhon, L. J.; Marks, T. J.; Hersam, M. C. *Nano Lett.* **2014**, *14* (12), 6964−6970.
(21) Doganov, R. A.; O'Farrell, E. C. T.; Koenig, S. P.; Yeo, Y.; Ziletti, A.; Carvalho, A.; Campbell, D. K.; Coker, D. F.; Watanabe, K.; Taniguchi, T.; Neto, A. H. C.; Özyilmaz, B. *Nat. Commun.* **2015**, *6*, 6647.
(22) Na, J.; Lee, Y. T.; Lim, J. A.; Hwang, D. K.; Kim, G.-T.; Choi, W. K.; Song, Y.-W. *ACS Nano* **2014**, *8* (11), 11753−11762.
(23) Avsar, A.; Vera-Marun, I. J.; Tan, J. Y.; Watanabe, K.; Taniguchi, T.; Castro Neto, A. H.; Özyilmaz, B. *ACS Nano* **2015**, *9*, 4138−4145.
(24) Wang, H.; Wang, X.; Xia, F.; Wang, L.; Jiang, H.; Xia, Q.; Chin, M. L.; Dubey, M.; Han, S. *Nano Lett.* **2014**, *14* (11), 6424−6429.
(25) Haratipour, N.; Robbins, M. C.; Koester, S. J. *IEEE Electron Device Lett.* **2015**, *36* (4), 411−413.
(26) Xiang, D.; Han, C.; Wu, J.; Zhong, S.; Liu, Y.; Lin, J.; Zhang, X.-A.; Ping Hu, W.; Özyilmaz, B.; Neto, A. H. C.; Wee, A. T. S.; Chen, W. *Nat. Commun.* **2015**, *6*, 6485.
(27) Ziletti, A.; Carvalho, A.; Campbell, D. K.; Coker, D. F.; Castro Neto, A. H. *Phys. Rev. Lett.* **2015**, *114* (4), 046801.
(28) Ziletti, A.; Carvalho, A.; Trevisanutto, P. E.; Campbell, D. K.; Coker, D. F.; Castro Neto, A. H. *Phys. Rev. B: Condens. Matter Mater. Phys.* **2015**, *91* (8), 085407.
(29) Boukhvalov, D. W.; Rudenko, A. N.; Prishchenko, D. A.; Mazurenko, V. G.; Katsnelson, M. I. *Phys. Chem. Chem. Phys.* **2015**, *17* (23), 15209−15217.
(30) Hu, T.; Hong, J. *J. Phys. Chem. C* **2015**, *119*, 8199−8207.
(31) Kulish, V. V.; Malyi, O. I.; Persson, C.; Wu, P. *Phys. Chem. Chem. Phys.* **2015**, *17*, 992−1000.
(32) Seixas, L.; Carvalho, A.; Castro Neto, A. H. *Phys. Rev. B: Condens. Matter Mater. Phys.* **2015**, *91* (15), 155138.
(33) Sui, X.; Si, C.; Shao, B.; Zou, X.; Wu, J.; Gu, B.-L.; Duan, W. *J. Phys. Chem. C* **2015**, *119*, 10059−10063.
(34) Hashmi, A.; Hong, J. *J. Phys. Chem. C* **2015**, *119* (17), 9198−9204.
(35) Hohenberg, P. *Phys. Rev.* **1964**, *136* (3B), B864−B871.
(36) Kohn, W.; Sham, L. J. *Phys. Rev.* **1965**, *140* (4A), A1133−A1138.
(37) Soler, J. M.; Artacho, E.; Gale, J. D.; García, A.; Junquera, J.; Ordejón, P.; Sánchez-Portal, D. *J. Phys.: Condens. Matter* **2002**, *14* (11), 2745−2779.
(38) Padilha, J. E.; Fazzio, A.; da Silva, A. J. R. *Phys. Rev. Lett.* **2015**, *114* (6), 066803.
(39) Kim, J.; Baik, S. S.; Ryu, S. H.; Sohn, Y.; Park, S.; Park, B.-G.; Denlinger, J.; Yi, Y.; Choi, H. J.; Kim, K. S. *Science (Washington, DC, U. S.)* **2015**, *349* (6249), 723−726.
(40) Tan, J. Y.; Avsar, A.; Balakrishnan, J.; Koon, G. K. W.; Taychatanapat, T.; O'Farrell, E. C. T.; Watanabe, K.; Taniguchi, T.; Eda, G.; Castro Neto, A. H.; Özyilmaz, B. *Appl. Phys. Lett.* **2014**, *104* (18), 183504.
(41) Castellanos-Gomez, A.; Buscema, M.; Molenaar, R.; Singh, V.; Janssen, L.; van der Zant, H. S. J.; Steele, G. A. *2D Mater.* **2014**, *1* (1), 011002.
(42) Doganov, R. A.; Koenig, S. P.; Yeo, Y.; Watanabe, K.; Taniguchi, T.; Özyilmaz, B. *Appl. Phys. Lett.* **2015**, *106* (8), 083505.
(43) Island, J. O.; Steele, G. A.; van der Zant, H. S. J.; Castellanos-Gomez, A. *2D Mater.* **2015**, *2* (1), 011002.
(44) Tosun, M.; Chuang, S.; Fang, H.; Sachid, A. B.; Hettick, M.; Lin, Y.; Zeng, Y.; Javey, A. *ACS Nano* **2014**, *8* (5), 4948−4953.
(45) Yu, L.; Zubair, A.; Santos, E. J. G.; Zhang, X.; Lin, Y.; Zhang, Y.; Palacios, T. *Nano Lett.* **2015**, *15* (8), 4928−4934.
(46) Su, Y.; Kshirsagar, C. U.; Robbins, M. C.; Haratipour, N.; Koester, S. J. *2D Mater.* **2016**, *3*, 011006.
(47) Troullier, N.; Martins, J. L. *Phys. Rev. B: Condens. Matter Mater. Phys.* **1991**, *43* (3), 1993−2006.
(48) Monkhorst, H. J.; Pack, J. D. *Phys. Rev. B* **1976**, *13* (12), 5188−5192.
(49) Perdew, J. P.; Burke, K.; Ernzerhof, M. *Phys. Rev. Lett.* **1996**, *77* (18), 3865−3868.
(50) Grimme, S. *J. Comput. Chem.* **2006**, *27* (15), 1787−1799.



DOI: 10.1021/acs.nanolett.5b03278
*Nano Lett.* 2016, 16, 2145−2151